

Reduced Auger Recombination in Single CdSe/CdS Nanorods by One-Dimensional Electron Delocalization

Freddy T. Rabouw,[†] Per Lunnemann,^{‡,§} Relinde J. A. van Dijk-Moes,[†] Martin Frimmer,^{‡,||} Francesca Pietra,[†] A. Femius Koenderink,[‡] and Daniël Vanmaekelbergh^{†,*}

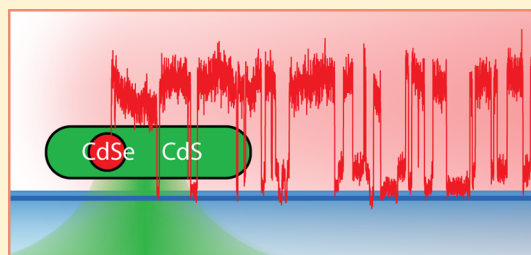
[†]Condensed Matter and Interfaces, Debye Institute for Nanomaterials Science, Princetonplein 1, 3584 CC Utrecht, The Netherlands

[‡]Center for Nanophotonics, FOM Institute AMOLF, Science Park 104, 1098 XG Amsterdam, The Netherlands

S Supporting Information

ABSTRACT: Progress to reduce nonradiative Auger decay in colloidal nanocrystals has recently been made by growing thick shells. However, the physics of Auger suppression is not yet fully understood. Here, we examine the dynamics and spectral characteristics of single CdSe-dot-in-CdS-rod nanocrystals. These exhibit blinking due to charging/discharging, as well as trap-related blinking. We show that one-dimensional electron delocalization into the rod-shaped shell can be as effective as a thick spherical shell at reducing Auger recombination of the negative trion state.

KEYWORDS: Nanocrystal, colloidal quantum dot, nanorod, blinking, trion, Auger recombination



Random switching, or “blinking”, between bright and dark states is a phenomenon generally observed in fluorescent colloidal nanocrystal quantum dots (QDs) when examined at the single-emitter level.^{1,2} The presence of dark states drastically reduces the efficiency of colloidal QDs, for example, in LEDs, lasers, and solar cells, in bioimaging, or as reliable single-photon sources. Blinking is commonly understood in terms of the charging/discharging model.³ According to this model a dark period is initiated if one charge carrier of a photoexcited exciton is trapped at the QD surface or ejected into the surrounding matrix. The remaining carrier quenches photoemission of subsequent excitons by opening a non-radiative Auger recombination pathway, in which it accepts the exciton recombination energy. Many recent experimental findings have been explained in terms of the charging/discharging model.^{4–12} However, there are experimental results that pose a challenge to this model.^{13–15} Galland et al. have proposed that in addition to charging/discharging, there may be a second blinking mechanism related to surface traps.¹⁶

Recently, a potential solution to the problem of blinking was presented with the introduction of colloidal QDs of CdSe with a thick CdS shell.^{4,17} In this system, lower-intensity periods are no longer completely dark but still have approximately 20–30% brightness compared to high-intensity periods. The unusual brightness of lower-intensity periods has been ascribed to suppression of nonradiative Auger recombination in the trion (charged exciton) state. In addition, relatively high biexciton quantum efficiencies^{18,19} have been found in these core/shell QDs, also ascribed to slow Auger rates. However, the physical origin of Auger suppression has not yet been clearly identified,²⁰ mainly because in thick-shell QDs several potentially important properties are combined: a smooth carrier confinement potential due to core/shell interface

alloying,^{21–23} electron delocalization into the CdS shell, and increased spatial separation between the emitting core and the nanocrystal surface.¹² The latter property combined with a temperature-dependent band offset has been invoked¹² to explain the observation of slow Auger rates at cryogenic temperatures.^{6,12,24,25} Moreover, different authors do not even agree on the sign of the charge of the unusually bright trion state.^{5–7,10,11,16,25} Clearly, blinking and Auger suppression are not yet entirely understood.

Here, we investigate single CdSe/CdS dot-in-rod structures, nanorods (NRs) of CdS with a spherical CdSe core. These NRs are presently of high interest due to the easy synthesis procedure, their high brightness, and photostability. Moreover, they have recently been identified as promising single-photon emitters,²⁶ which can exhibit efficient negative trion emission.²⁷ They have a peculiar shape and band structure, such that holes are tightly confined to the core, while electrons can delocalize along the long direction of the CdS rod.^{28–36} We show that partial electron delocalization in the long direction of the CdS rod can be as effective as the more “conventional” thick spherical CdS shell^{4,17} for the suppression of Auger decay.

We perform detailed studies on single NRs using a combination of photoluminescence (PL) decay and time-resolved spectral measurements under ambient conditions. We quantify the rate constants and binding energies of the different states of the NRs. From a comparison of the experimental results with quantum-mechanical effective-mass calculations, we specifically identify lower-intensity periods with the negative

Received: July 25, 2013

Revised: August 26, 2013

Published: September 6, 2013

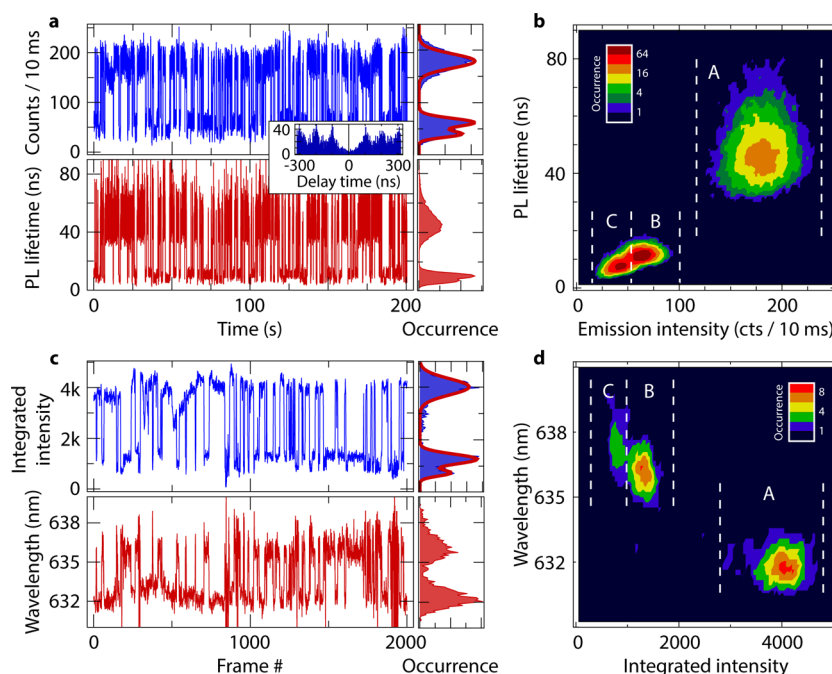


Figure 1. (a) The intensity trace (top) and PL lifetime trace (bottom) of a single CdSe/CdS NR measured over 200 s using TCSPC and corresponding histograms (right). We used a time binning of 10 ms. The background counts are less than 0.1 cts/10 ms. Inset: the absence of a zero-delay peak in the photon–photon correlation proves that we are looking at a single NR. (b) The fluorescence-lifetime-intensity-distribution (FLID) constructed from the data in panel a, indicating in logarithmic color scale the frequency of occurrence for a combination of emission intensity and PL lifetime. The three distinct states A, B, and C are highlighted by dashed lines. (c) The intensity trace (top) and emission wavelength trace (bottom) of the same single NR measured on the spectrometer, and corresponding histograms (right). Each spectral frame is obtained by integration over 20 ms. (d) The EWID constructed from the data in panel c, indicating in color scale the frequency of occurrence for a combination of integrated intensity and emission wavelength. Again, states A, B, and C are highlighted by dashed lines.

trion state, in accordance with Tenne et al.²⁷ Remarkably, we find that our NRs are comparable to the thick-shell (10–12 monolayers) QDs in terms of quantum efficiency of the trion state, although the CdSe core is only covered by a very thin shell of CdS (3 monolayers) in the short direction of the NR. We conclude that electron delocalization in just one dimension (i.e., along the length of the NR) is sufficient to achieve efficient suppression of nonradiative Auger recombination. More precisely, we measure an average Auger lifetime of 11 ns over 18 single NRs, which is an order of magnitude longer than the lifetime of the negative trion state in spherical thin-shell CdSe/CdS QDs.³⁷ Our observations illustrate that Auger losses in colloidal nanocrystals can effectively be reduced by wave function engineering in specifically designed heterostructures.

This Letter is organized as follows: first we describe in detail how we quantify the dynamics and transition energies of the states involved in the blinking of a single NR. Using simple effective-mass calculations we then identify that each NR shows blinking between a neutral exciton and a negative trion state. Next, we briefly discuss the two types of blinking statistics observed among the different NRs (exponential and power-law), which indicate that in some NRs there is trap-related blinking in addition to exciton-trion blinking. Finally, we explain the relatively high quantum efficiency of the negative trion state arguing that Auger recombination is suppressed by the smooth Coulomb potential that binds the partially delocalized electron to the core-confined hole.

Characterization of Bright and Gray States. We investigate single colloidal NRs with a CdSe dot core of 3.2 nm diameter and a CdS rod shell of 5.6 nm diameter and 21 nm length (with 10% size polydispersity; see also Figure 4a).

The characterization of a single NR consists of two parts (see Methods for technical details). First, we do time-correlated single-photon counting (TCSPC) for 200 s in a Hanbury Brown-Twiss setup, allowing for the simultaneous acquisition of an intensity trace over time scales of seconds to minutes, the photon–photon correlation function $g^{(2)}$, and PL decay curves. We divide the total measurement time into time bins of 10 ms. For each time bin, we extract the number of photon counts, and the PL lifetime by fitting a single-exponential decay function to the histogram (165 ps binning) of delay times between pump pulse and arrival of a fluorescence photon, using a maximum-likelihood routine.³⁸ Subsequently, we flip a mirror in the detection arm of our setup and record a series of 2000 emission spectra each with an integration time of 20 ms. We fit each 20 ms emission frame to a single Gaussian and extract (1) the integrated emission intensity, and (2) the peak emission wavelength.

We have examined a total of 18 single NRs. Figure 1a shows the results of TCSPC measurements on one of them: the intensity and extracted PL lifetime traces, and the corresponding histograms. The vanishing photon–photon correlation at zero time delay (inset) proves that we are examining a single emitter, and that biexciton emission does not obscure our measurements³⁹ (see Supporting Information Discussion 1 for details). We see that the NR exhibits both intensity blinking and PL lifetime blinking, that is, random switching between well-defined values for these parameters. Nevertheless, the emission intensity never approaches the background value of 0.1 cts/10 ms so the NR always remains emissive. Furthermore, the blinking behavior does not change over the measurement time of 200 s, hence the NR does not degrade. In the intensity

histogram (Figure 1a, top right) we distinguish three states: a bright state with mean emission intensities of $M_A = 179$ cts/10 ms that we label “A”, and two lower-intensity “gray” states ($M_B = 63$ cts/10 ms, $M_C = 41$ cts/10 ms) that we label “B” and “C”. The good correspondence to a Poissonian intensity distribution (red line) for each of the three peaks in the histogram indicates that three well-defined states are involved. In order to examine the correlation between intensity and PL lifetime we combine the two traces and obtain the fluorescence-lifetime-intensity-distribution (FLID)⁴⁰ of the NR, as presented in Figure 1b. The logarithmic color scale quantifies the frequency of occurrence for a combination of emission intensity and PL lifetime. We notice from the FLID that the bright state A has a long PL lifetime, while the two distinct gray states B and C have shorter PL lifetimes.

Continuing, we focus on the spectral measurements performed on the same NR and at the same laser power. Figure 1c shows the integrated intensity and emission wavelength traces and the corresponding histograms. Still, no degradation of the NR occurs. Intensity and emission wavelength blinking are clearly visible. Again, three peaks appear in the intensity histogram (Figure 1c, top right). These peaks have the same relative mean intensities and weights (obtained from a fit to three Gaussians; red line) as those in the intensity histogram constructed from the TCSPC data (Figure 1a). Clearly, in the spectral measurements we resolve and identify the same three states A, B, and C as in the TCSPC measurements. Combination of the intensity and emission wavelength traces yields the emission-wavelength-intensity-distribution (EWID; Figure 1d). We see that the emission wavelengths of states B and C are very close. In fact, state B and C are indistinguishable based on the wavelength histogram alone (Figure 1c) due to fit uncertainties and the fact that each of the states may exhibit spectral diffusion^{41,42} comparable to the separation between B and C. Still, the EWID (Figure 1d) unambiguously shows the presence of two distinct states B and C that differ slightly in terms of emission wavelength.

In the following, we aim to identify the different states from their PL decay and spectral characteristics. Therefore, we assign each time bin from the TCSPC series (Figure 1a) and each spectral frame from the spectral series (Figure 1c) to state A, B, or C, based on the clear definition of the three states in the FLID (Figure 1b) and EWID (Figure 1d). We obtain the state-averaged PL decay curves and emission spectra, as presented in Figure 2. PL decay curves (Figure 2a) are excellently fitted with a single-exponential decay. The spectra (Figure 2b) are asymmetrically broadened toward the low-energy side and are

fitted to a series of phonon replicas with a fixed spacing of 26 meV (see the Methods section for details). Table 1 summarizes the best-fit values for PL lifetime, PL decay amplitude, and emission wavelength (i.e., zero-phonon peak energy E_0), as well as the photon count rates obtained from the fit to the intensity histogram (Figure 1a; see above).

Next, we wish to determine the quantum efficiency, η , of the gray states, and quantify the competition between radiative and nonradiative recombination that leads to the unusually high brightness. To this end, we use our fit results from Table 1, and inspired by previous works^{7,10} we employ two different methods to estimate radiative and nonradiative contributions to the total decay. In both methods, one assumes that the quantum efficiency of the bright state $\eta_A = 1$ ^{7,43–45} (we have measured it to be at least 87%⁴⁶) and that the excitation rate of the emitter is the same in each state (see Supporting Information Discussion 2 for comments). In the first method,⁷ one retrieves the quantum efficiency of gray state i from the photon count rate M : $\eta_i/\eta_A = M_i/M_A$. In the second method,¹⁰ one obtains the radiative decay rate $\tau_{r,i}^{-1}$ of state i from the PL decay amplitude: $\tau_{r,i}^{-1}/\tau_{r,A}^{-1} = A_i/A_A$. Table 1 shows the estimates of quantum efficiency and radiative and nonradiative decay rates obtained using the two different methods. Strikingly, the quantum efficiencies of the gray states (B and C) for this NR are very high, even comparable to those encountered in thick-shell CdSe/CdS QDs.^{7,9}

To test whether the results are reproducible we examined 17 more single NRs. The Supporting Information present a full overview of the characteristics of each of the 18 NRs. All NRs exhibit a clear gray state B similar to the NR discussed in detail above. The characteristics of the lowest-intensity state, however, are much less uniform. Four NRs do not show a third state at all, but only two states A and B. In the other NRs, the lowest-intensity states can be divided into two groups: five NRs have one bright (A) and two gray states (B and C) as encountered for the NR discussed above (Figure 1). On the other hand, nine NRs show a bright (A) and a gray (B) state in addition to a lowest-intensity state which is almost dark (<3 cts/10 ms). First, we will focus on characterization and identification of the omnipresent gray state B. Later, we tentatively assign the different lowest-intensity states observed.

Figure 3 summarizes the characteristics of gray state B of the 18 single NRs examined. Figure 3a presents the correlation between the radiative lifetimes of states A and B, estimated using method 1 (via the photon count rate; open circles) and method 2 (via the PL decay amplitude; closed disks). We see that the radiative lifetime is shorter in the gray state B than in the bright state A by a factor of $1.51(\pm 0.21)$ (mean \pm standard deviation). Figure 3b shows the emission energies of states A and B. We see that the emission of the gray state B is consistently lower in energy than the emission of the bright state A by $10(\pm 7)$ meV. In Figure 3c, we plot the radiative and nonradiative lifetimes of state B [indicating the two methods for parameter estimation with open circles (method 1) and closed disks (method 2), as in Figure 3a]. We see that in all NRs the radiative decay of state B is competitive with nonradiative decay, resulting in quantum efficiencies as high as $25(\pm 10)\%$. Supporting Information Figure S1 shows that the trends observed in Figure 3 are robust to more conservative estimates of $\eta_A = 0.75$ and a 20% lower excitation rate of state B compared to state A, rather than $\eta_A = 1$ and equal excitation rates.

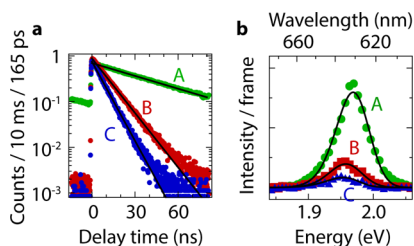


Figure 2. (a) PL decay curves (semilog scale) of the states A (green), B (red), and C (blue). Solid black lines are single exponential fits. (b) Emission spectra of the states A (green circles), B (red squares), and C (blue triangles). Solid lines are fits to a series of phonon replicas with a fixed spacing of 26 meV. See the Methods section for details of the fitting procedure.

Table 1. Characteristics of the Three Distinct States A, B, and C^a

		state A	state B	state C
Fit Results				
photon count rate M (cts/10 ms)		179.5 ± 0.9	62.6 ± 0.8	40.8 ± 0.9
PL lifetime τ (ns)		46.4 ± 0.3	11.19 ± 0.08	7.04 ± 0.07
PL decay amplitude A (cts/10 ms/165 ps)		0.632 ± 0.003	0.939 ± 0.009	0.730 ± 0.010
emission energy E_0 (meV)		1974 ± 3	1961 ± 5	1960 ± 11
Parameter Estimates				
quantum efficiency	(1)	100*	34.9 ± 0.5	22.7 ± 0.5
η (%)	(2)	100*	35.9 ± 0.5	17.5 ± 0.3
radiative lifetime	(1)	46.4 ± 0.3	32.1 ± 0.5	31.0 ± 0.8
τ_r (ns)	(2)	46.4 ± 0.3	31.2 ± 0.4	40.1 ± 0.6
nonrad. lifetime	(1)	∞	17.19 ± 0.23	9.11 ± 0.13
τ_{nr} (ns)	(2)	∞	17.45 ± 0.23	8.54 ± 0.11
Assignment		X^0	X^-	

^a Fit results were obtained from fits to the experimental TCSPC and spectral data. Estimates of quantum efficiency, radiative, and nonradiative lifetimes are made using two methods, which are described in the text and specified in parentheses in the first column. Error margins represent 95% confidence intervals as obtained from the fitting errors. Additional uncertainty of a few percent stems from the choice of thresholds for the assignment of time slices to a state. For the parameter estimates, origins of error are discussed in the Supporting Information Discussion 2. * = by assumption.

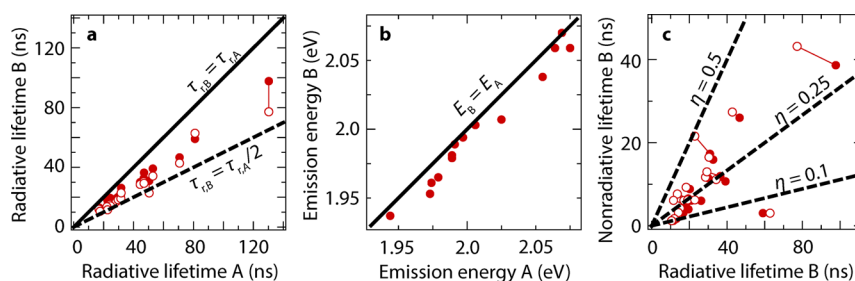


Figure 3. Overview of the characteristics of the bright state A and gray state B for 18 single NRs. Estimates obtained by method 1 (via the photon count rate; see text for details) are given in open circles, those obtained by method 2 (via the PL decay amplitude; see text for details) in closed disks. Solid lines connect symbols that belong to the same NR, i.e. the results of method 1 and 2. Error margins are typically <1% (see Table 1) and within the size of the symbols. (a) The correlation between the radiative lifetimes of the bright state A (the neutral exciton X^0) and the gray state B (the negative trion X^-). Radiative decay is faster in the gray state than in the bright state by a factor $1.51(\pm 0.21)$ (mean \pm standard deviation). (b) The correlation between the emission energies of the bright and the gray state. Emission from the gray state is lower in energy by $10(\pm 7)$ meV. (c) The correlation between the radiative and nonradiative lifetimes of the gray state. The resulting quantum efficiency of the gray state is $25(\pm 10)\%$.

The increased radiative decay rate of the gray state compared to the bright state (Figure 3a) is a strong indication in favor of the charging/discharging model. Radiative decay rates increase with the number of charge carriers in the system.^{10,16} Alternative models, which invoke the presence of trap-related nonradiative decay channels during low-intensity periods,^{47,48} cannot account for an increase in radiative decay rate. Hence, we conclude that bright periods (state A) correspond to the neutral state of the emitter, where emission originates from the uncharged exciton X^0 . During gray periods (state B) the emitter is charged, and emission originates from a trion, that is, a charged exciton.

The Effect of Electron Delocalization. In previous studies, there has been disagreement on the sign of the trion charge associated with the observed gray states.^{5,7,10,11,16} Here, by comparison of the experimental results to quantum-mechanical effective-mass calculations we will show that the gray state B in our NRs is the negative trion state. To this end, we calculate radiative decay rates and transition energies of the neutral exciton X^0 , negative trion X^- , and positive trion X^+ . Details of the calculation method can be found in the Supporting Information Methods. Briefly, we model the NR as the three-dimensional system depicted in Figure 4a [the actual NRs examined (Figure 4b) exhibit 10% size polydisper-

sity]. The CdSe core is assumed to act as an infinite potential well for the hole.⁴⁹ The electron, on the other hand, is free to find the optimal extent of (de)localization under the influence of Coulomb attraction of the hole, a small conduction band (CB) offset, the different effective masses in CdS and CdSe, and (for the case of the two electrons in X^-) Coulomb repulsion of the other electron.

Figure 4c,d presents the results of our effective-mass calculations: the transition energies (c) and the radiative lifetimes (d) of the neutral exciton X^0 , the negative trion X^- and the positive trion X^+ . On the x-axis, we varied the CB offset between 0⁵⁰ and 300 meV⁵¹ (with the CdSe core having the lower CB minimum), since its value is not well established in literature and is assumed to depend for example on strain in the nanocrystal.⁵² The sensitivity of the CB offset may also partially explain the widespread in radiative lifetimes that we find in our system experimentally and has been found for single thick-shell CdSe/CdS QDs.¹⁰ The calculated binding energies of X^- and X^+ are consistent with previous assignments of emission spectra of ensembles of charged QDs,^{53,54} as well as single QDs at cryogenic temperatures.^{6,24} The experimental transition energy difference between state B and state A is 10 meV (Figure 3b), in close agreement with the calculated 10–19 meV difference (Figure 4c; depending on the value of the CB offset) between

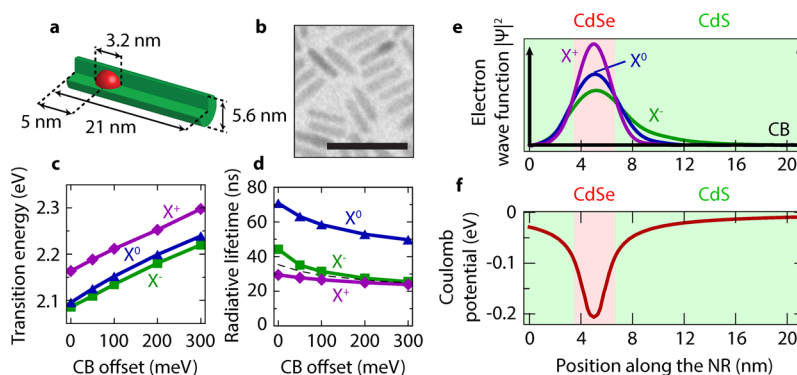


Figure 4. (a) The dimensions of the model NR used for the effective-mass calculation. The spherical CdSe core of 3.2 nm diameter is embedded in a cylindrical CdS rod of 5.6 nm diameter and 21 nm length, and positioned with its center at 5 nm from one end of the rod. (b) A transmission electron micrograph of the nanorods. Scale bar is 40 nm. (c) The transition energy and (d) radiative lifetime of X^+ , X^0 , and X^- , calculated for different values of CB offset. The dashed line in (d) represents radiative decay which is exactly twice faster than in X^0 . (e) The normalized electron wave functions $|\Psi|^2$ in the different states, showing the variable extent of electron localization (calculated for a CB offset of 0 meV). The thick black line represents the CB potential experienced by the electron (not including Coulomb interactions) with an infinite potential outside the NR. (f) The soft potential well experienced by the electron due to electron–hole Coulomb attraction. See the Supporting Information Methods for details of the calculation method.

X^- and X^0 (see also Supporting Information Discussion 3). Furthermore, the experimental ratio of radiative lifetimes $\tau_{r,A}/\tau_{r,B}$ is 1.51 (Figure 3a), in fair agreement with the calculated ratio of $\tau_{r,X^0}/\tau_{r,X^-} = 1.60$ –1.95 (Figure 4d). For the positive trion X^+ , on the other hand, the calculations predict characteristics that are totally inconsistent with gray state B: approximately 60 meV higher transition energy, and a shorter radiative lifetime by a factor 2.1–2.4 compared to X^0 . Accordingly, we identify the bright state A and the gray state B as the neutral exciton X^0 and the negative trion X^- , respectively.

Remarkably, we find, experimentally and theoretically, that the negative trion has a slower radiative decay rate than predicted by statistical scaling relations which are often used for rate estimates.^{10,11,37} Scaling of the radiative rate with the number of recombination pathways would lead to a radiative rate of X^- that is twice faster than for X^0 , since the hole has twice as many electrons with which to recombine.¹⁰ However, the electron–hole overlap integrals in X^- and X^0 are different. Figure 4d shows the electron wave functions in the X^+ , X^0 , and X^- states calculated for a CB offset of 0 meV. Clearly, the extent of electron localization varies significantly between the states. More precisely, electron–electron Coulomb repulsion enhances delocalization in X^- compared to X^0 . Because of a smaller electron–hole overlap integral, radiative recombination via either pathway in X^- is slower than in X^0 . As a result, the radiative decay for X^- is faster by a factor smaller than two (see Figure 4d). Indeed, we have measured that $\tau_{r,A}/\tau_{r,B} = 1.51$, which is 25% off the value of $\tau_{r,X^0}/\tau_{r,X^-} = 2$ that one would expect from statistical scaling.¹⁰ The 25% deviation is a direct manifestation of electron delocalization.

Analysis of the Lowest-Intensity States. Next, we focus on the lowest-intensity states, which are intrinsically hard to characterize due to the low signal. We can divide the 18 NRs examined (Supporting Information) into two groups. Group 1 (containing NRs #1, 2, 4, 5, 6, 7, 10, 17, 18) shows only bright \leftrightarrow gray blinking, that is, the brightness does not fall below 20% of the brightest state. In five of these (NRs #4, 5, 6, 10, 17) there are two distinct gray states B and C (Figure 1), while the other four appear to have only one gray state B. Group 2, on the other hand, contains NRs (the other nine) showing bright

\leftrightarrow gray blinking in addition to a “dark state” with emission intensity < 3 cts/10 ms. This dark state, that we label “D”, is very different from the gray states B and C as we will show below. Figure 5a presents the intensity histograms of two NRs, representative for group 1 (left) and group 2 (right). We have labeled the different states A, B, C, and D according to their emission intensities. We clearly see that only the NR on the right exhibits a dark state D with < 3 cts/10 ms. Figure 5b shows the blinking statistics of these two NRs (left and right). We plot the bright/dim duration probability distributions^{55,56} using the threshold intensities indicated by the dashed lines in Figure 5a. The two NRs have qualitatively different duration probability distributions, which are representative for the other NRs of the respective groups. NRs without a dark state (group 1; Figure 5 left) show exponential distributions, while those with a dark state (group 2; Figure 5 right) show power-law distributions. On the basis of the bright/dim statistics, and on the PL decay and spectral properties, we will now make assignments, first for the gray state C (Figure 5a left) and then for the dark state D (Figure 5a right).

The characteristics of gray state C (Table 1) differ only slightly from the X^- state B: roughly 30% lower emission intensity, 30% shorter PL lifetime, and equal emission energy. Furthermore, the exponential statistics associated with a state C (Figure 5 left) indicates that $A \leftrightarrow C$ blinking involves an Auger-assisted charging mechanism following the occasional creation of a biexciton and with a well-defined rate constant.⁵⁷ In fact, exponential statistics have been found for $X^0 \leftrightarrow X^-$ blinking in thick-shell CdSe/CdS QDs.^{10,16} We propose that gray state C is a negative trion X^- that differs from the X^- state B by the location where the ejected hole resides.⁴⁰ Indeed, the charging/discharging model for blinking involves ejection of a charge (here, the hole) that resides on the surface or in the environment of the NR for some time before returning. Because of the anisotropic shape of the NRs, there may be two possible types of locations for the ejected hole to reside, giving rise to two negative trion states X^- with similar but slightly different characteristics.

We can model the effect of the ejected hole by a single positive point charge on the NR surface in our effective-mass model. We put a point charge at the tip or at the side (nearest

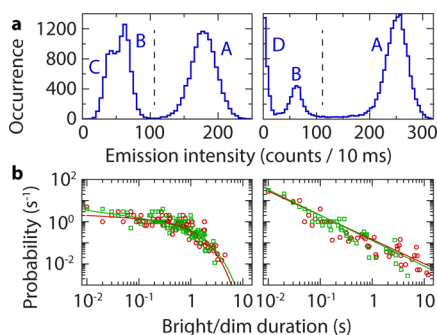


Figure 5. (a) Intensity histograms of a NR from the first group (with a gray state C; left) and of a NR from the second group (with a dark state D; right). Binning: 5 counts. (b) The corresponding probability duration distributions of the bright periods (state A; red circles), and dim periods (states B + C/D; green squares) for the NR from group 1 (left), and the NR from group 2 (right). The intensity thresholds used are depicted by dashed lines in panel a.

to the core) of the NR, 1 nm from the surface. We can then compare the resulting transition energy and radiative lifetime of the X^- state to the above calculations in which we neglected the ejected hole. Using a conduction band offset of -100 meV the changes are -3 meV and -1.6 ns for the charge at the tip, and -5 meV and -1.6 ns for the charge at the side. Hence, the ejected hole may indeed be responsible for the small distinction between the B and C states. However, the effects are so small that we cannot make statements about exactly where the ejected hole resides in the experiment.

The different statistics (Figure 5b) imply that two completely different mechanisms underlie $A \leftrightarrow D$ blinking and $A \leftrightarrow B,C$ blinking. Moreover, state D (NRs from group 2; Figure 5 right) has very different properties from states B and C: very low emission intensity ($<3\%$ compared to the X^0 state) and very short PL lifetime ($1-2$ ns). In addition, PL decay curves of state D have a lower amplitude (see Supporting Information) than those of the X^0 state. This indicates that state D is, in fact, not a charged state, since an extra charge would lead to an increased radiative rate and with that a higher PL decay amplitude for state D (see above). Hence, we tentatively assign blinking to state D to the opening and closing of trap states. The trap model has been used before to explain the power-law statistics encountered in many single emitters (but which we find exclusively in NRs with a state D), including conventional QDs.^{2,55,56} Our results seem to confirm those of Galland et al.¹⁶ and Tenne et al.²⁷ who found that blinking can be due to combination of charging/discharging and opening/closing of trap states, but that the two blinking mechanisms are distinct in terms of the blinking statistics. Note, however, that our state D has a short PL lifetime (indicating that traps capture charge carriers from the lowest energy exciton) whereas in ref 16 the PL lifetime of the trap-related low-intensity state has a long PL lifetime (indicating that traps only capture hot charge carriers that have not yet relaxed to the band edge). Reference 27 does not investigate the PL dynamics of the trap-related state.

Suppression of Auger Recombination. We now return to the main focus of this paper which is the properties of the negatively charged state B. We recognize the nonradiative lifetimes of state B (Figure 3c) as Auger lifetimes of X^- . Auger recombination is slow enough that radiative decay can compete with it, resulting in X^- quantum efficiencies in our NRs (25%) as high as those observed in thick-shell CdSe/CdS QDs with 12 monolayer (5 nm) thick shells.^{7,9} This finding is consistent with

the recent observations of reduced blinking²⁶ and efficient negative trion emission²⁷ in CdSe/CdS NRs. However, it is remarkable if we consider that in our system the CdSe core is covered by a cylindrical CdS shell that is only 3 monolayers thin in the direction perpendicular to the long NR axis. The average Auger lifetime of 11 ns (distributed from 1.2 to 40.9 ns) is still an order of magnitude longer than observed in spherical thin-shell (2–3 monolayers) CdSe/CdS QDs.³⁷ Apparently, merely one-dimensional electron delocalization results in efficient Auger suppression in the negative trion state.

Our NRs are different from thick-shell QDs in terms of two important properties that have previously been argued to be responsible for a suppression of Auger recombination. First, the NRs have only a small separation between the emitting core and the outer surface. Apparently, charge carriers reaching the outer surface of a nanocrystal do not necessarily lead to efficient Auger decay. This finding seems to contrast with the model of Javaux et al.¹² who attribute the suppression of Auger recombination in core/shell QDs at cryogenic temperatures to surface assisted Auger decay combined with temperature-dependent band offsets. Second, (unintentional) interfacial alloying^{8,22,23} is most likely absent in our NRs, as evidenced by the low biexciton quantum efficiency (see Figure 1a) and the short reaction time during synthesis (a few minutes²⁹ versus many hours for the thick-shell QDs¹⁷). We conclude that interfacial alloying is also no strict requirement to achieve suppression of Auger decay. We must, however, point out that we cannot exclude other subtle differences between our NRs and thick-shell QDs in terms of strain fields^{52,58–60} or stacking faults.⁶¹ More in-depth experimental⁶² and theoretical work will have to be performed to quantify these differences and their potential effect on charge carrier dynamics.

We can qualitatively explain the occurrence of suppressed Auger decay in our NRs in terms of the simple theoretical model of Cragg and Efros.²¹ They argued that the Auger recombination rate roughly scales with high spatial-frequency components of the charge carrier wave functions, and that those high-frequency components are reduced in amplitude if the confinement potential experienced by the excess carrier is smoothed or “softened”.^{21,63} On the basis of this argumentation, Auger suppression has been linked to soft confinement potentials due to core/shell interface alloying.^{8,22,23} Interestingly, in our NRs the confinement potential experienced by the electron is also soft but for another reason. The extent of electron localization is namely dictated by long-range Coulomb attraction of the hole, which is tightly confined to the core. The softness of the Coulomb confinement potential is evident from Figure 4f. Soft confinement leads to partial electron delocalization that allows for substantial radiative recombination (which does require electron–hole overlap), while restraining high-frequency components in the electron wave function (limiting Auger decay). As a consequence, in our NRs the negative trion has a high quantum efficiency. In fact, Auger suppression in thick-shell CdSe/CdS QDs may also in large part be enabled by the softness of the electron–hole Coulomb attraction. Indeed, also in the thick-shell systems the extent of electron delocalization is set by the Coulomb potential of the core-confined hole. However, this effect has so far mostly been overlooked in favor of the interface alloying model.²¹

Our findings point toward a new design rule for nanocrystals with reduced Auger recombination. As an alternative method to core/shell interface alloying,^{8,22,23} a soft confinement potential

can also result from electron delocalization and long-range electron–hole Coulomb interaction (Figure 4f). Generalizing, we suggest that Auger recombination in nanostructures may be suppressed if the extent of confinement of the excess carrier is mainly set by Coulomb attraction of opposite charges rather than spatial confinement (as in conventional or thin-shell QDs). Indeed, relatively slow biexciton Auger decay has recently been found in spherical “type-II” InP/CdS QDs,⁶⁴ where Coulomb interaction is an important factor determining the shape of charge carrier wave functions. Moreover, Auger decay is slow in bulk semiconductors,^{65,66} where Coulomb interaction is the only interaction that binds electron–hole pairs.

We must emphasize that while our NRs are an excellent model system to study the effect of delocalization on Auger recombination, only Auger decay of the negative trion X^- is suppressed. Auger decay of excitonic states with an excess hole (biexcitons X_2 and possibly positive trions X^+) is still efficient (see also Supporting Information Discussion 1) because holes experience hard confinement by the large CdSe/CdS valence band offset. New nanostructure designs, aimed at increasing the importance of Coulomb interactions for the extent of confinement of both electrons and holes, may lead to suppression of Auger losses for all excitonic states. Wave function engineering promises to be a good strategy to achieve this goal, facilitated by the tremendous progress made in recent years in controlling the shape and composition of colloidal heterosystems.⁶⁷ As an example, in Supporting Information Figure S2 we propose a colloidal nanostructure in which both electrons and holes can partially delocalize and which promises to have suppressed Auger recombination in all excitonic states but efficient radiative recombination due to the presence of direct electron–hole overlap.

To summarize, we have identified the negative trion state in blinking CdSe/CdS NRs based on its PL decay and spectral characteristics (i.e., faster radiative decay by a factor 1.51 and a lower transition energy by 10 meV compared to the neutral exciton). These characteristics are a direct consequence of the shape and band alignment of our heterostructure. Furthermore, we have explained the blinking behavior involving multiple states as encountered in many of the NRs. Most importantly, we have quantified the suppression of nonradiative Auger recombination in the negative trion state, which leads to the quantum efficiency as high as 25%. Strikingly, this value is comparable to those reported for thick-shell CdSe/CdS QDs.^{7,9} We attribute Auger suppression to the fact that the extension of the electron wave function is mainly dictated by a soft Coulomb confinement potential. We envision that our work will lead to new strategies for the minimization of nonradiative Auger losses that currently form a major obstacle for the application of colloidal nanocrystals in devices.

Methods. The NRs examined in this study were synthesized following the method of Carbone et al.²⁹ and then coated with a thin layer of silica following ref 68. The NRs have an ensemble quantum yield of 74%, measured using an integrating sphere. The silica layer serves as protection against photo bleaching.⁶⁹ Furthermore, we found that silica-coated NRs cluster less than bare ones. We deposited the NRs on a glass slide from a dilute dispersion in ethanol. We used the microscope setup depicted and described in ref 70. All measurements were performed in ambient conditions. Single NRs were excited with 10 ps, 10 MHz, 532 nm linearly polarized pulses generated by a frequency doubled Nd:YVO₄

laser, through an oil immersion objective with a magnification of 100 and numerical aperture (NA) 1.4. We used a laser power of 200 nW focused to a diffraction-limited spot. From the count rate of the high-intensity state of single NRs (approximately 20 kHz), the estimated collection efficiency of our microscope setup (10%) and detection efficiency of our detectors (10%), we estimate that at this laser intensity we create $\langle N \rangle \approx 0.2$ excitons per laser pulse. This corresponds well to the value of $\langle N \rangle \approx 0.1$ excitons estimated from the absorption cross-section of the NRs ($\sigma_{\text{abs}} \approx 10^{-15} \text{ cm}^2$ at 532 nm).^{30,71} Fluorescence light was collected through the same objective used for excitation and was separated from laser reflections using a long-pass filter with a cutoff at 590 nm. For timing and photon–photon correlation measurements, we used a Hanbury Brown–Twiss setup with two ID Quantique id100–20 ULN avalanche photodiodes (APDs; dark counts <10 Hz) connected to a timing card (DPC 230, Becker & Hickl GmbH) with 165 ps time resolution. Spectral measurements were done with an Acton Research SpectraPro 2300i spectrograph equipped with a PIXIS:100B back-illuminated Si CCD array by Princeton Instruments. We remark that the CCD camera used for spectral measurements required a few ms read-out time between successive frames.

We used single exponential decay functions to fit the state-resolved PL decay curves (Figure 2a and panels c of the Supporting Information)

$$I(t) = A \exp\left(\frac{-t}{\tau}\right) \quad (1)$$

where the fit parameters A and τ are the PL decay amplitude and PL lifetime, respectively. We used a maximum-likelihood routine for the fits,³⁸ assuming Poissonian statistics. A flat background was not included since the dark count rate of our detectors is <10 cts/s. For PL decay curves with a longer lifetime tail, we fitted only to the single exponential early time signal. The values of the PL decay amplitudes A given (Table 1 and the summarizing tables in the Supporting Information) are corrected for the relatively short laser repetition period ($T = 100 \text{ ns}$) of our setup compared to the PL lifetimes ($\tau = 5\text{--}50 \text{ ns}$): $A \rightarrow A/[1 + \exp(-T/\tau)]$. A correction is needed because the tail of a PL decay curve with $t > T$ is counted toward the early time signal ($t \rightarrow t - T$), as clearly visible in the PL decay curve of state A (Figure 2a and panels c in the Supporting Information); the signal at negative delay is the tail of the PL decay that extends over longer than 100 ns.

State-averaged emission spectra (Figure 2b and panels e in the Supporting Information) are asymmetrically broadened toward the red side due to exciton–phonon coupling. They were fitted to a series of phonon replicas at fixed energy intervals of $\epsilon_{\text{LO}} = 26 \text{ meV}$ (the longitudinal optical phonon energy in CdSe) using a nonlinear least-squares method

$$I(E) = I_0 \sum_{n=0}^S \frac{S^n}{n!} \exp\left[-\frac{1}{2} \left(\frac{E - E_0 + n\epsilon_{\text{LO}}}{\sigma}\right)^2\right] \quad (2)$$

Here the fit parameters I_0 , E_0 , σ , and S are the peak amplitude, zero-phonon peak energy, peak width, and Huang–Rhys factor, respectively. We obtained typical values for the Huang–Rhys factor of $S = 0.3\text{--}1.2$. The choice for a Gaussian line shape for each phonon replica is set by broadening due to coupling to lower-energy phonon modes. We find typical values for the peak width of $\sigma = 30\text{--}40 \text{ meV}$.

■ ASSOCIATED CONTENT

■ Supporting Information

Supplementary data of all the single NRs examined; a description of the effective-mass model used; a discussion of the methods used to estimate rate constants, including the assumptions made; the proposal of a ternary nanocrystal that should have reduced Auger recombination in all excitatonic states; a discussion of the biexciton quantum efficiency; a discussion of the transition energies. This material is available free of charge via the Internet at <http://pubs.acs.org>.

■ AUTHOR INFORMATION

Corresponding Author

*E-mail: d.vanmaekelbergh@uu.nl.

Present Addresses

[§](P.L.) DTU Fotonik, Department of Photonics Engineering, Technical University of Denmark, DK- 2800 Kongens Lyngby, Denmark.

^{||}(M.F.) Photonics Laboratory, ETH Zürich, 8093 Zürich, Switzerland.

Notes

The authors declare no competing financial interest.

■ ACKNOWLEDGMENTS

This work is part of the research program of the “Stichting voor Fundamenteel Onderzoek der Materie (FOM)”, which is financially supported by the “Nederlandse Organisatie voor Wetenschappelijk Onderzoek (NWO)”. P.L. gratefully acknowledges the Carlsberg Foundation for financial support. A.F.K. gratefully acknowledges an NWO-Vidi grant for financial support.

■ REFERENCES

- (1) Nirmal, M.; Dabbousi, B. O.; Bawendi, M. G.; Macklin, J. J.; Trautman, J. K.; Harris, T. D.; Brus, L. E. *Nature* **1996**, *383*, 802–804.
- (2) Frantsuzov, P.; Kuno, M.; Jankó, B.; Marcus, R. A. *Nat. Phys.* **2008**, *4*, 519–522.
- (3) Efros, A.; Rosen, M. *Phys. Rev. Lett.* **1997**, *78*, 1110–1113.
- (4) Mahler, B.; Spinicelli, P.; Buil, S.; Quelin, X.; Hermier, J.-P.; Dubertret, B. *Nat. Mater.* **2008**, *7*, 659–664.
- (5) Gómez, D. E.; Van Embden, J.; Mulvaney, P.; Fernée, M. J.; Rubinsztein-Dunlop, H. *ACS Nano* **2009**, *3*, 2281–2287.
- (6) Fernée, M. J.; Littleton, B. N.; Rubinsztein-Dunlop, H. *ACS Nano* **2009**, *3*, 3762–3768.
- (7) Spinicelli, P.; Buil, S.; Quelin, X.; Mahler, B.; Dubertret, B.; Hermier, J.-P. *Phys. Rev. Lett.* **2009**, *102*, 136801.
- (8) Wang, X.; Ren, X.; Kahen, K.; Hahn, M. A.; Rajeswaran, M.; Maccagnano-Zacher, S.; Silcox, J.; Cragg, G. E.; Efros, A. L.; Krauss, T. D. *Nature* **2009**, *459*, 686–689.
- (9) Malko, A. V.; Park, Y.-S.; Sampat, S.; Galland, C.; Vela, J.; Chen, Y.; Hollingsworth, J. A.; Klimov, V. I.; Htoon, H. *Nano Lett.* **2011**, *11*, 5213–5218.
- (10) Galland, C.; Ghosh, Y.; Steinbrück, A.; Hollingsworth, J. A.; Htoon, H.; Klimov, V. I. *Nat. Commun.* **2012**, *3*, 908.
- (11) Qin, W.; Shah, R. A.; Guyot-Sionnest, P. *ACS Nano* **2012**, *6*, 912–918.
- (12) Javaux, C.; Mahler, B.; Dubertret, B.; Shabaev, A.; Rodina, A. V.; Efros, A. L.; Yakovlev, D. R.; Liu, F.; Bayer, M.; Camps, G.; Biadala, L.; Buil, S.; Quelin, X.; Hermier, J.-P. *Nat. Nanotechnol.* **2013**, *8*, 206–212.
- (13) Zhao, J.; Nair, G.; Fisher, B. R.; Bawendi, M. G. *Phys. Rev. Lett.* **2010**, *104*, 157403.
- (14) Rosen, S.; Schwartz, O.; Oron, D. *Phys. Rev. Lett.* **2010**, *104*, 157404.
- (15) Cordones, A. A.; Bixby, T. J.; Leone, S. R. *Nano Lett.* **2011**, *11*, 3366–3369.
- (16) Galland, C.; Ghosh, Y.; Steinbrück, A.; Sykora, M.; Hollingsworth, J. A.; Klimov, V. I.; Htoon, H. *Nature* **2011**, *479*, 203–207.
- (17) Chen, Y.; Vela, J.; Htoon, H.; Casson, J. L.; Werder, D. J.; Bussian, D. A.; Klimov, V. I.; Hollingsworth, J. A. *J. Am. Chem. Soc.* **2008**, *130*, 5026–5027.
- (18) Zhao, J.; Chen, O.; Strasfeld, D. B.; Bawendi, M. G. *Nano Lett.* **2012**, *12*, 4477–4483.
- (19) Park, Y.-S.; Ghosh, Y.; Chen, Y.; Piryatinski, A.; Xu, P.; Mack, N. H.; Wang, H.-L.; Klimov, V. I.; Hollingsworth, J. A.; Htoon, H. *Phys. Rev. Lett.* **2013**, *110*, 117401.
- (20) Hollingsworth, J. A. *Chem. Mater.* **2013**, *25*, 1318–1331.
- (21) Cragg, G. E.; Efros, A. L. *Nano Lett.* **2010**, *10*, 313–317.
- (22) García-Santamara, F.; Brovelli, S.; Viswanatha, R.; Hollingsworth, J. A.; Htoon, H.; Crooker, S. A.; Klimov, V. I. *Nano Lett.* **2011**, *11*, 687–693.
- (23) Bae, W. K.; Padilha, L. A.; Park, Y.-S.; McDaniel, H.; Robel, I.; Pietryga, J. M.; Klimov, V. I. *ACS Nano* **2013**, *7*, 3411–3419.
- (24) Louyer, Y.; Biadala, L.; Tamarat, P.; Lounis, B. *Appl. Phys. Lett.* **2010**, *96*, 203111.
- (25) Fernée, M. J.; Sinito, C.; Louyer, Y.; Potzner, C.; Nguyen, T.-L.; Mulvaney, P.; Tamarat, P.; Lounis, B. *Nat. Commun.* **2012**, *3*, 1287.
- (26) Pisanello, F.; Leménager, G.; Martiradonna, L.; Carbone, L.; Vezzoli, S.; Desfonds, P.; Cozzoli, P. D.; Hermier, J.-P.; Giacobino, E.; Cingolani, R.; De Vittorio, M.; Bramati, A. *Adv. Mater.* **2013**, *25*, 1974–1980.
- (27) Tenne, R.; Teitelboim, A.; Rukenstein, P.; Dyschel, M.; Mokari, T.; Oron, D. *ACS Nano* **2013**, *7*, 5084–5090.
- (28) Talapin, D. V.; Koeppel, R.; Go, S.; Kornowski, A.; Lupton, J. M.; Rogach, A. L.; Benson, O.; Feldmann, J.; Weller, H. *Nano Lett.* **2003**, *3*, 1677–1681.
- (29) Carbone, L.; Nobile, C.; De Giorgi, M.; Sala, F. D.; Morello, G.; Pompa, P.; Hytch, M.; Snoeck, E.; Fiore, A.; Franchini, I. R.; Nadasan, M.; Silvestre, A. F.; Chiodo, L.; Kudera, S.; Cingolani, R.; et al. *Nano Lett.* **2007**, *7*, 2942–2950.
- (30) Talapin, D. V.; Nelson, J. H.; Shevchenko, E. V.; Aloni, S.; Sadtler, B.; Alivisatos, A. P. *Nano Lett.* **2007**, *7*, 2951–2959.
- (31) Lupo, M. G.; Della Sala, F.; Carbone, L.; Zavelani-Rossi, M.; Fiore, A.; Lüer, L.; Polli, D.; Cingolani, R.; Manna, L.; Lanzani, G. *Nano Lett.* **2008**, *8*, 4582–4587.
- (32) Sitt, A.; Della Sala, F.; Menagen, G.; Banin, U. *Nano Lett.* **2009**, *9*, 3470–3476.
- (33) Saba, M.; Minniberger, S.; Quochi, F.; Roither, J.; Marceddu, M.; Gocalinska, A.; Kovalenko, M. V.; Talapin, D. V.; Heiss, W.; Mura, A.; Bongiovanni, G. *Adv. Mater.* **2009**, *21*, 4942–4946.
- (34) Zavelani-Rossi, M.; Lupo, M. G.; Tassone, F.; Manna, L.; Lanzani, G. *Nano Lett.* **2010**, *10*, 3142–3150.
- (35) She, C.; Demortière, A.; Shevchenko, E. V.; Pelton, M. J. *Phys. Chem. Lett.* **2011**, *2*, 1469–1475.
- (36) Kunneman, L. T.; Zanella, M.; Manna, L.; Siebbeles, L. D. A.; Schins, J. M. J. *Phys. Chem. C* **2013**, *117*, 3146–3151.
- (37) Jha, P. P.; Guyot-Sionnest, P. *ACS Nano* **2009**, *3*, 1011–1015.
- (38) Bajzer, Z.; Therneau, T. M.; Sharp, J. C.; Prendergast, F. G. *Eur. Biophys. J.* **1991**, *20*, 247–262.
- (39) Nair, G.; Zhao, J.; Bawendi, M. G. *Nano Lett.* **2011**, *11*, 1136–1140.
- (40) Zhang, K.; Chang, H.; Fu, A.; Alivisatos, A. P.; Yang, H. *Nano Lett.* **2006**, *6*, 843–847.
- (41) Empedocles, S. A.; Norris, D. J.; Bawendi, M. G. *Phys. Rev. Lett.* **1996**, *77*, 3873–3876.
- (42) Neuhauser, R. G.; Shimizu, K. T.; Woo, W. K.; Empedocles, S. A.; Bawendi, M. G. *Phys. Rev. Lett.* **2000**, *85*, 3301–3304.
- (43) Brokmann, X.; Coolen, L.; Dahan, M.; Hermier, J. *Phys. Rev. Lett.* **2004**, *93*, 107403.
- (44) Leistikow, M. D.; Johansen, J.; Kettlerij, A. J.; Lodahl, P.; Vos, W. L. *Phys. Rev. B* **2009**, *79*, 045301.
- (45) Kwadrin, A.; Koenderink, A. F. *J. Phys. Chem. C* **2012**, *116*, 16666–16673.

- (46) Lunnemann, P.; Rabouw, F. T.; van Dijk-Moes, R. J. A.; Pietra, F.; Vanmaekelbergh, D.; Koenderink, A. F. *ACS Nano* **2013**, *7*, 5984–5992.
- (47) Frantsuzov, P. A.; Marcus, R. A. *Phys. Rev. B* **2005**, *72*, 155321.
- (48) Frantsuzov, P. A.; Volkán-Kacsó, S.; Jankó, B. *Phys. Rev. Lett.* **2009**, *103*, 207402.
- (49) Shabaev, A.; Rodina, A. V.; Efros, A. L. *Phys. Rev. B* **2012**, *86*, 205311.
- (50) Müller, J.; Lupton, J. M.; Lagoudakis, P. G.; Schindler, F.; Koeppel, R.; Rogach, A. L.; Feldmann, J.; Talapin, D. V.; Weller, H. *Nano Lett.* **2005**, *5*, 2044–2049.
- (51) Steiner, D.; Dorfs, D.; Banin, U.; Sala, F. D.; Manna, L.; Millo, O. *Nano Lett.* **2008**, *8*, 2954–2958.
- (52) Luo, Y.; Wang, L.-W. *ACS Nano* **2010**, *4*, 91–98.
- (53) Oron, D.; Kazes, M.; Shweky, I.; Banin, U. *Phys. Rev. B* **2006**, *74*, 115333.
- (54) Saba, M.; Aresti, M.; Quochi, F.; Marceddu, M.; Loi, M. A.; Huang, J.; Talapin, D. V.; Mura, A.; Bongiovanni, G. *ACS Nano* **2013**, *7*, 229–238.
- (55) Kuno, M.; Fromm, D. P.; Hamann, H. F.; Gallagher, A.; Nesbitt, D. J. *J. Chem. Phys.* **2001**, *115*, 1028–1040.
- (56) Cordones, A. A.; Bixby, T. J.; Leone, S. R. *J. Phys. Chem. C* **2011**, *115*, 6341–6349.
- (57) Peterson, J. J.; Nesbitt, D. J. *Nano Lett.* **2009**, *9*, 338–345.
- (58) Morello, G.; Della Sala, F.; Carbone, L.; Manna, L.; Maruccio, G.; Cingolani, R.; De Giorgi, M. *Phys. Rev. B* **2008**, *78*, 195313.
- (59) Smith, A. M.; Mohs, A. M.; Nie, S. *Nat. Nanotechnol.* **2009**, *4*, 56–63.
- (60) Smith, E. R.; Luther, J. M.; Johnson, J. C. *Nano Lett.* **2011**, *11*, 4923–4931.
- (61) Hughes, S. M.; Alivisatos, A. P. *Nano Lett.* **2013**, *13*, 106–110.
- (62) Bertoni, G.; Grillo, V.; Brescia, R.; Ke, X.; Bals, S.; Catellani, A.; Li, H.; Manna, L. *ACS Nano* **2012**, *6*, 6453–6461.
- (63) Climente, J. I.; Movilla, J. L.; Planelles, J. *Small* **2012**, *8*, 754–759.
- (64) Dennis, A. M.; Mangum, B. D.; Piryatinski, A.; Park, Y.-S.; Hannah, D. C.; Casson, J. L.; Williams, D. J.; Schaller, R. D.; Htoon, H.; Hollingsworth, J. A. *Nano Lett.* **2012**, *12*, 5545–5551.
- (65) Kharchenko, V. A.; Rosen, M. *J. Lumin.* **1996**, *70*, 158–169.
- (66) Klimov, V. I.; Mikhailovsky, A. A.; McBranch, D. W.; Leatherdale, C. A.; Bawendi, M. G. *Science* **2000**, *287*, 1011–1013.
- (67) De Mello Donegá, C. *Chem. Soc. Rev.* **2011**, *40*, 1512–1546.
- (68) Koole, R.; Van Schooneveld, M. M.; Hilhorst, J.; Donegá, C. D. M.; Hart, D. C.; Van Blaaderen, A.; Vanmaekelbergh, D.; Meijerink, A. *Chem. Mater.* **2008**, *20*, 2503–2512.
- (69) Kobayashi, Y.; Misawa, K.; Kobayashi, M.; Takeda, M.; Konno, M.; Satake, M.; Kawazoe, Y.; Ohuchi, N.; Kasuya, A. *Colloids Surf. A* **2004**, *242*, 47–52.
- (70) Frimmer, M.; Chen, Y.; Koenderink, A. F. *Phys. Rev. Lett.* **2011**, *107*, 123602.
- (71) Leatherdale, C. A.; Woo, W.-K.; Mikulec, F. V.; Bawendi, M. G. *J. Phys. Chem. B* **2002**, *106*, 7619–7622.